Postprint of: Wodtke M., Litwin W., Water-lubricated stern tube bearing - experimental and theoretical investigations of thermal effects, Tribology International, Vol. 153 (2021), 106608, DOI: 10.1016/j.triboint.2020.106608.

Water-lubricated stern tube bearing - experimental and theoretical investigations of thermal effects

Wodtke M.[a] and Litwin W.[b]

[a] *Gdansk University of Technology, Faculty of Mechanical Engineering, 80-233 Gdansk, Narutowicza 11/12, Poland*

[b] *Gdansk University of Technology, Faculty of Ocean Engineering and Ship Technology, 80-233 Gdansk, Narutowicza 11/12, Poland*

Keywords: stern tube bearing, thermal effects, water lubrication, experimental tests

Abstract:

The paper presents research results of thermal phenomena accompanying operation of a water-lubricated stern tube bearing with axial grooves. Experimental tests revealed, that intensity of forced axial flow has strong influence on bush temperature. Numerical simulations focused on investigation of the thermal phenomena under operation of water-lubricated journal bearing showed, that restricted axial flow promotes backflow of the water from bearing's side zones through the grooves. The backflow temperature is higher than the supply temperature since under the conditions of restricted forced axial flow, it is impacted mainly by the temperature of the water outflow from the gap, which is higher due to the shearing of lubricating film. This effect causes rise in the temperature of the bearing bush.

1 Introduction

Marine main shaft bearings are very crucial elements of the propulsion system of the ships. This type of bearing is usually made of relatively elastic materials (rubber, polymers) and equipped with internal open axial grooves that help maintain the forced water axial flow necessary for proper bearing operation (Fig. 1). Water axial flow supports lubrication and intensifies bearing cooling. According to bearing manufacturers' recommendations, the minimum axial water flow rate depends on its design and size and should be in the range of 0.15–0.30 litres per minute per millimetre of shaft diameter [1,2].

The safety of shipping depends, among other things, on the durability and reliability of shaft bearings. According to experience and the results of experimental investigations, the most common causes of bearing failures are:

- assembly errors resulting in stress concentration caused mostly by misalignment of the bushing and shaft [3–5],
- unfavourable internal bearing geometry, especially groove distribution around the perimeter [6,7],
- excessive bearing clearance and bushing shape errors due to assembly using a thermo-compression method (the bushing is cooled before installation; for most polymers, the thermal expansion coefficient is high, which helps shrink the bushing and easily install it in the housing) [1],
- unfavourable selection of bushing and shaft materials or severe operating conditions [8,9],
- presence of solid particles in the lubricant [10,11] or corrosion [12],

– improper lubrication or insufficient axial lubricant flow causing overheating of the bearing materials [2].

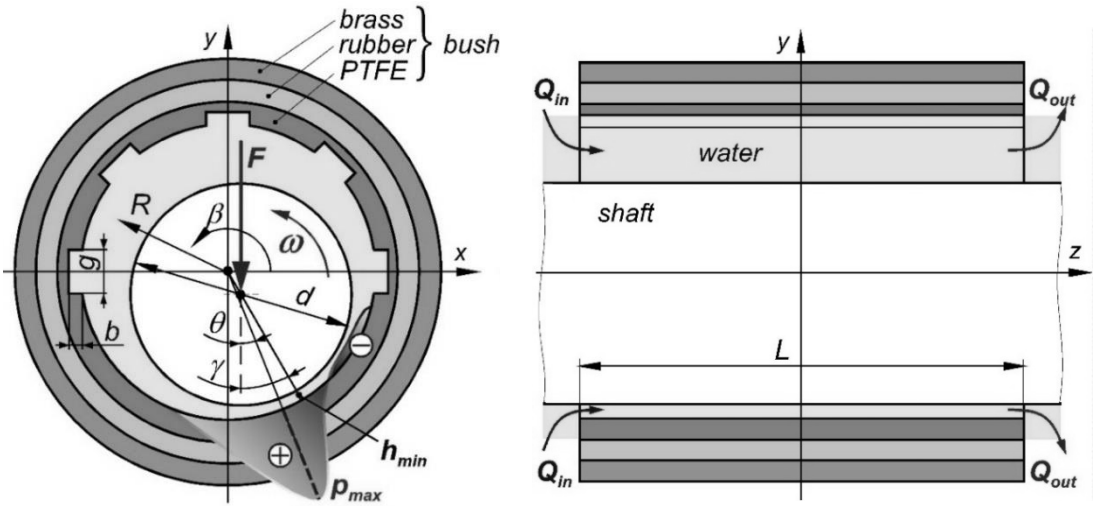

Fig. 1. Schematic operation of the water-lubricated journal bearing with axial grooves.

The final listed bearing failure reason is associated with thermal effects in the bearing system and, according to the authors' best knowledge, thermal effects were the subject of only a few studies so far. Experimental investigations were focused mainly on the effect of a temperature increase under bearing operation without axial water flow [2,13]. The results of those tests indicated a significant temperature increase of the bearing bushing. It was also proven that for some bearing designs, such operating conditions were unacceptable and the bearing was not able to operate with an appropriate margin of safety.

In the case of theoretical investigations of hydrodynamic water-lubricated bearings, the assumption of isothermal water flow in the film was taken very often [14–21]. In the case of analyses of water-lubricated thrust bearings that considered thermal effects under hydrodynamic lubrication [22–24], the predicted temperature increase depends on bearing design and operating conditions and can be significant. However, the results of these analyses cannot be transferred directly to journal bearings because the different contact area geometry (conformal contact in the case of journal bearings and flat in the case of thrust bearings) and pattern of water flow in the gap probably influences the course of thermal effects. In available papers that investigated the impact of temperature increase on the properties of water-lubricated journal bearings [25,26], the bushing was considered rigid or made of a relatively stiff material (e.g. steel). This is different compared to real industrial stern tube bearing applications, which are usually made of soft materials or their elasticity is provided by special bearing designs [27]. In addition, theoretical investigations were limited to plain cylindrical bearings, and consequently, the effect of axial water flow on bearing properties was not considered. Additionally, the shaft was usually not considered as a component of the bearing system that is able to transfer heat from the gap to the environment.

According to a review of the available literature, the course of thermal effects during the operation of water-lubricated hydrodynamic bearings with open axial grooves, with special attention to the influence of axial flow, have not been studied experimentally and theoretically so far.

This paper investigates the problem of the thermal phenomena accompanying stern tube bearing operation. The main goal of this research is to understand the key factors influencing the origin and course of thermal effects, including the influence of forced axial flow through the bearing. For this purpose, experimental tests were carried out using a test stand that allows for testing full-scale bearings under conditions of various axial water flow rates. Analyses were carried out for a three-layer water-lubricated bearing design with five axial grooves located in the upper part of the sleeve, which was selected based on previous results from extensive experimental investigations [6,13]. Experimental studies were supplemented with theoretical analysis of the bearing. A series of numerical simulations of the bearing system was carried out using the FSI (*fluid-solid interaction*) method, which combines CFD (*computational fluid dynamics*) and CSM (*computational solid mechanics*) and allows for complex thermo-elastohydrodynamic (TEHD) analysis of water-lubricated bearings. Calculations were carried out for the hydrodynamic mode of bearing operation and several sets of assumptions for bearing system behaviour (adiabatic flow, with and without sleeve deformations, with an adiabatic shaft or comprehensive TEHD analysis) to investigate their influence on the predicted bearing performance and thermal effects. Using the results of both experimental and theoretical investigations, conclusions were drawn concerning the thermal effects course in bearings with axial grooves and the influence of forced axial water flow on bearing operation.

2 Research object

An industrial three-layer journal bearing was selected as an object of investigation. This bearing type is accepted by ship classification societies and is used in the shipbuilding industry. It is composed of three layers (each 5 mm thick), made of different materials, PTFE, Rubber (NBR) and Brass. The tested bearing after assembly in the test stand housing (in the form of a heavy and massive sleeve) is shown in Fig. 2.

Fig. 2. Side view of the tested stern tube water-lubricated bearing assembled in the test-stand housing.

Bearing geometry and operating conditions are summarized in Table 1. Its geometrical parameters are typical for stern tube bearings with a length/diameter ratio of 2 and relatively large diametral clearance (~0.4 mm; 4‰), which is typical for water-lubricated bearings. The bearing was tested at three levels of shaft speed (1000, 2000 and 3000 rpm) and four levels of specific pressure (0.2, 0.4, 0.6 and 0.8 MPa). At each combination of applied load/speed,

the water flow was changed, according to the procedure described in the next section, starting at 15 l/min. The operating conditions during tests were similar to those in industrial applications. The bearing was lubricated by pure water supplied from one side (see Q_{in} in Fig. 1). In real applications, filtered outboard water or freshwater circulating in a more complex, sealed and closed system can be used. It is also worth noting that lubrication grooves were only in the upper half of the bushing, as shown in Fig. 2.

Table 1. Bearing data and operating conditions (selected symbols shown in Fig. 1).

parameter	symbol	value/comment
shaft material	-	steel X10CrNi18-8 (AISI 301)
bushing material	-	3 layer (PTFE / NBR / Brass)
bushing geometry	-	5 grooves in the upper part
grooves dimensions	g x b	12 mm x 3.5 mm
shaft diameter / bushing length	d / L	100 mm / 200 mm
diametral clearance (meas. at 20°C)	c	~ 0.4 mm (cylindricity deviation)
shaft rotational speed	n	1000, 2000, 3000 rpm
bearing load / specific pressure	F / p_m	4 - 16 kN / 0.2 - 0.8 MPa
operating temperature	T	20°C (water inlet, ambient)
water flow rate	Q_{in}	15 l/min (max.)

3 Research methodology

3.1 Experimental tests

A schematic of the test stand for research on water-lubricated bearings is shown in Fig. 3.

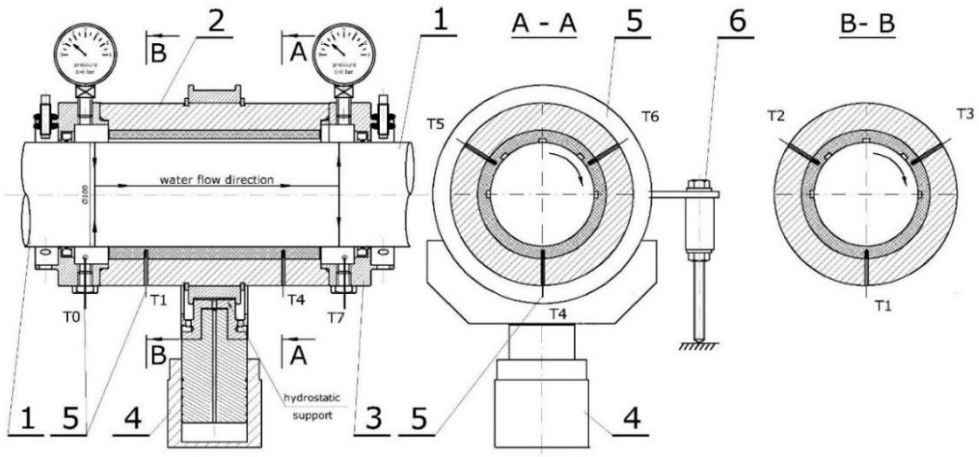

Fig. 3. Test stand cross-section; 1- main shaft, 2- housing, 3- cover with seals, 4- loading system 5- thermocouples (T0–T7), 6- friction force sensor.

The main shaft of the test stand is supported by two rolling element bearings. Between them, there is a bearing test unit. An electric motor and AC controller were used for the drive. It has a 15 kW power output and a starting torque of about 60 Nm. On the shaft (1), the tested bushing was mounted in a massive housing (2). Water was supplied to the bearing through one of the covers (Fig. 3 part no. 3), causing forced axial water flow, which is typical for ship propeller shaft bearings. The tested bearing was closed on both sides using covers equipped with sealing rings. Lip seals were used on both sides. The tension springs were removed to lower movement resistance of the seals, reduce the losses and the heat generation in the

friction zone. The load was exerted by a hydraulic cylinder via a hydrostatic bearing (4). Oil pressure measurement in the hydrostatic system was used to adjust and control the load applied to the bearing. Separation of the system exerting the load and the test stand housing using a hydrostatic film assured self-aligning and enabled precise measurements of the friction force with the use of cantilever beam (200 mm long) and force sensor (6). The recorded data can be further used to obtain bearing friction torque (with a correction of losses in shaft sealings) and, consequently, friction coefficient. Unfortunately, this support method also has a disadvantage. During the tests, there is no control over the position of the bushing axis with respect to the shaft axis.

For the research, the bearing sleeve was equipped with 6 type K thermocouples (OD 1 mm) placed in two cross-sections (B-B → sensors marked T1-T3 and A-A → T4-T6, see Fig. 3). The thermocouples were fixed in radial blind holes 2 mm under the bearing sliding surface. Moreover, two additional thermocouples were applied to monitor water temperature at both ends of the bearing, T0 at the water inlet to the housing and T7 at the water drain from the housing. The temperature sampling frequency was 1 Hz. The assessed accuracy of the measurements using the applied thermocouples was ± 0.5°C. Water flow through the bearing was set using an adjusting valve. A flow meter was installed at the supply water line to control the flow rate. During all tests, the temperature of the supply water was 20±1°C, the same as the hall temperature. A view of the test stand under operation is presented in Fig. 4.

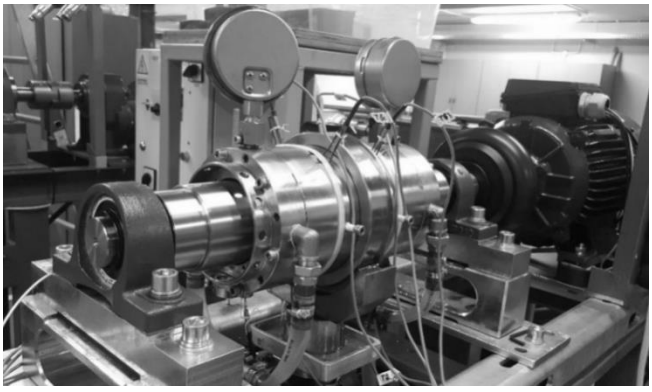

Fig. 4. Test rig for water-lubricated bearings under operation.

The applied testing procedure was the same for all analysed operating conditions and axial flows. First, the assumed value of axial flow through the bearing was set, and then, the shaft was driven and the bearing was loaded to the selected value of speed and radial force. During operation, temperature changes at the monitored bearing system points were recorded. The next test at other operating conditions was performed after cooling the system to the initial temperature (usually the following day). It was assumed that one test at certain operating conditions took no more than 40 minutes. Presented in Fig. 5 are sample trends of measured temperature increase under different bearing operating conditions. In most typical cases, at the end of the test, water drain temperatures were stable (Fig. 5 a; cases A and B), similar to bushing temperatures (Fig. 5 b; case F), which was evidence that thermal equilibrium of the bearing system was obtained and axial water flow was sufficient for its safe operation. It was assumed that the test was 'passed' in such cases.

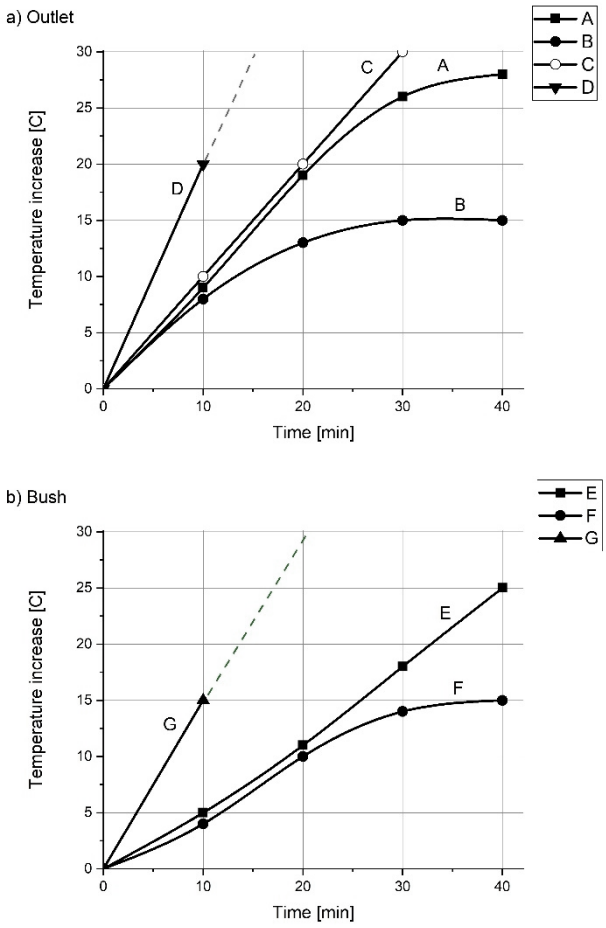

Fig. 5. Sample diagrams of temperature increase as a function of time; a) for water outlet; b) for bushing.

If the measured water temperature increased rapidly under operation (Fig. 5 a; C and D) or the bushing temperature increase was continuous without the tendency to reach a stable level (Fig. 5 b; case E and G), the test was stopped before the end and marked as 'not passed'. The planned axial water flow rate range was 0–15 l/min. For a given operating condition, measurements were started at the largest axial flow. Then, in the following tests, the flow was gradually reduced (usually by a factor around 2).

Interpretation of obtained results was summarised in the form of a diagram of safe bearing operation under limited lubrication. An example of such diagram for 2000 rpm case was presented in Fig. 6. The most important line is the boundary line, which divides the diagram into two parts - the upper one (including points belonging to the boundary line) contains ‘passed’ cases and the lower part contains ‘not passed’ cases, for which thermal stability was not observed. For selected boundary cases (points on boundary line between 'passed' and 'not passed' zones) measured temperature was not fully stabilized in 40 minutes, however showed clear trend to achieve stabilization. Such tests were also assumed as 'passed' in the case, when measured temperature increase was lower than 40^{o}C. This type of diagram seems very simple for interpretation and provides an easy method to assess bearing safety under operation with limited axial water flow.

It should be noted that operational conditions on the test stand are different than on a real stern tube bearing. In the case of the test rig, the conditions are harder because the starting

temperature is 20°C. In addition, the heat generated in the friction zone must be conducted into the surrounding air, which is a worse case than on a ship, where the surrounding water provides a much intensive cooling.

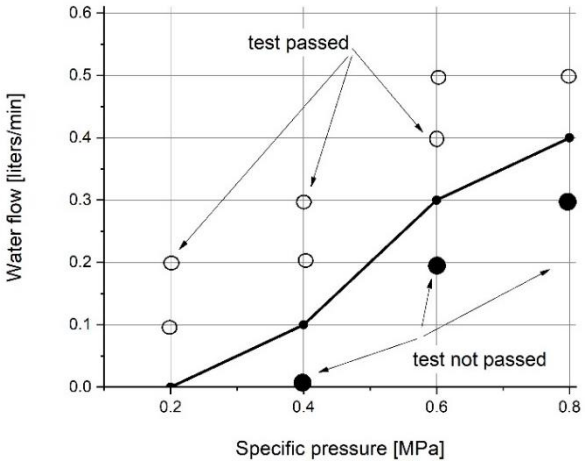

Fig. 6. Diagram of bearing safe operation under limited lubrication conditions (for 2000 rpm case).

3.2 Theoretical research

Theoretical analyses of the problem were carried out using the FSI technique implemented in the commercial ANSYS package [28]. This technique utilized a so-called *partitioned approach* to solving a governing set of equations with the use of two separate solvers for each physical field. The connection between fields relies on data transfer at common surfaces (FSI surfaces) in a series of iterations until a convergent solution is reached. FSI was applied with success for analysis of hydrodynamic bearing systems in many previously published works [29–34]. In the most general case, this technique allows for TEHD analysis of the bearing system, since it is possible (at FSI surfaces) to exchange information about temperature, heat flow, forces and deformations of the bearing components.

Within this research, the CFD CFX solver was utilized to analyse water flow (FVM solver; *finite volume method*) while the ANSYS mechanical solver was used for bearing component calculations (FEM solver; *finite element method*). Exchange of the loads between solvers, for the most advanced case of TEHD calculations for stern tube bearing, was carried out on two interaction surfaces. One surface was defined at the film and shaft interface (named FSI 1) and the other at film and bushing interface (FSI 2, also includes part of bushing end side surfaces with radius < 53.5 mm). As a result, comprehensive analyses of the hydrodynamic bearing system were carried out using the solution of general conservation equations of the flow (mass, momentum and energy) supplemented with turbulence and cavitation equations and equations of thermo-elastic deformation for the bushing (including its thermal expansion). For each case analysed computationally, the shaft equilibrium position under the given external load and speed was sought. The shaft, under the forces acting on it (external load and hydrodynamic force), moved from the initial position to the equilibrium position. Bearing bushing deformation (elastic and thermal due to pressure and thermal gradients) changed the gap geometry and pressure distribution, and thus, affected the equilibrium position. The theoretical approach flowchart is presented in Fig. 7.

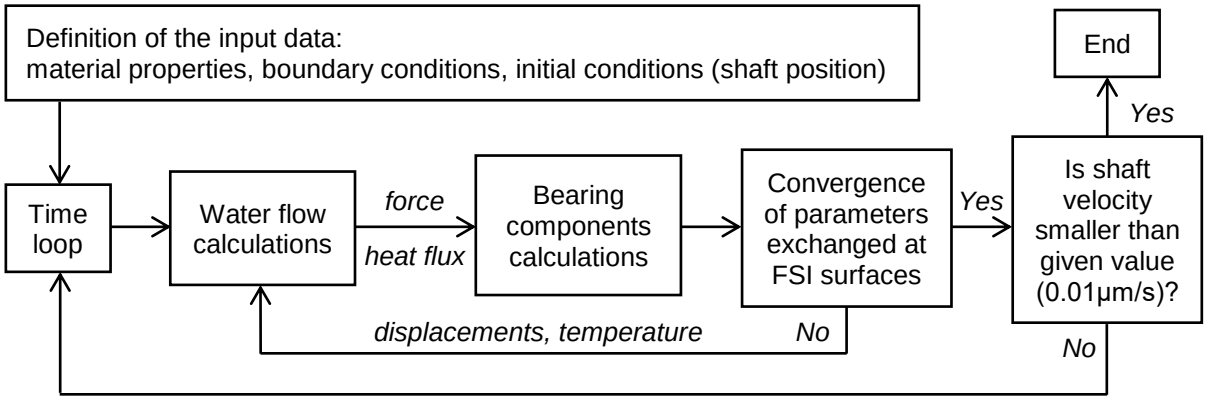

Fig. 7. Flowchart of the theoretical analysis.

In this research modelling was limited to: lubricating film (including axial grooves), side water flow zones in the bearing, sleeve and shaft. In a more general approach, it would be also necessary to include the test rig housing and its surrounding air to establish precise predictions of temperature distribution in the entire bearing system. This however would require enormous computer resources and for that reason is not commonly applied to hydrodynamic bearing investigations.

A detailed discussion of governing equations is not given in this paper since it can be found in other published works [28–30]. In the following subsections, details concerning the imposed boundary conditions and detailed assumptions for numerical models developed to analyse the fluid flow and thermo-mechanical phenomena in the bearing system are provided.

3.2.1. Water flow

The numerical grid for all fluid flow simulations with boundary conditions is shown in Fig. 8. It contains a thin fluid film, five axial grooves located in the upper part of the bushing (at 0–180° angular range) and additional fluid volumes at both axial ends of the bearing.

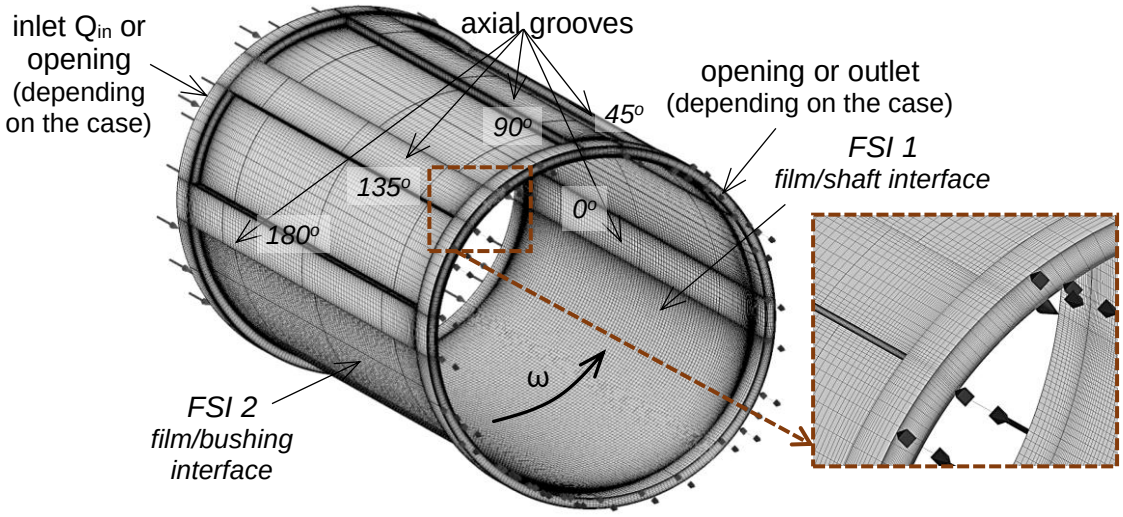

Fig. 8. Fluid flow grid (grooves identified with their angular position) and boundary conditions (marked schematically).

Due to presence of axial grooves, which disturb the flow in the gap and are a source of mixing and changes of flow direction, a turbulence model was included in the analysis (k – ω, SST turbulence model) with an automatic wall function. Initial results of simulations demonstrate,

that in almost the entire fluid volume, there exist preferable conditions for the occurrence of turbulence. Low water viscosity, relatively large bearing clearance and high shaft speed along with the presence of axial grooves, are the factors which promote turbulent flow in the bearing. In addition, two-phase flow with cavitation was also assumed due to the need to limit negative pressure values in the divergent part of the lubrication gap (Rayleigh-Plesset model, saturation pressure 3574 Pa, mean nucleation diameter 2 μm). For the modelling of cavitating flow, a homogeneous multiphase model was applied. That model assumes, that a flow field is shared by both phases (which have the same pressure, velocity and temperature fields). Comprehensive description of the cavitation model implemented in the numerical solver could be found in the work of Laukiavich et al. [30].

The material parameters for fluid flow simulation of water and water vapour are collected in Table 2. Exponential variations of the dynamic viscosity of the water with temperature were taken into account using Sutherland's formula (μ_{20} = 0.001 Pas, μ_{40} = 0.000653 Pas).

At the external front walls of the grid, boundary conditions were imposed, such as the inlet (with assumed axial flow Q_{in} at T_{in} = 20°C, turbulence intensity parameter 5%, volume fraction = 1) and (depending on the analysis case) opening (turbulence intensity parameter 5%, volume fraction = 1, opening temperature T_{op} = 20°C) or outlet (with relative average static pressure 0 Pa).

Table 2. Material properties assumed for fluid flow analysis.

parameter		Water	Water vapour
density	[kg/m^3]	997	0.0231
thermal conductivity	[W/mK]	0.6069	0.01854
specific heat	[J/kg K]	4181.7	1911.6
dynamic viscosity	[Pa s]	μ = f(T)	9.9 x 10^{-6}

Applied axial grid extensions (10 mm thick) allowed calculating fluid flow at the bushing edges, which could be local inflow or outflow depending on conditions in the film and grooves, instead of assuming it was uniform at the film side ends. At the film/shaft interface, angular velocity ω was imposed as a boundary condition. Depending on the case, one or two FSI surfaces were defined on fluid model walls (interface with the shaft and with the bushing) to transfer loads between solvers. The remaining external walls of the fluid grid were assumed adiabatic and stationary with the 'no-slip wall' condition. The fluid model (based on the results of previous mesh studies [31]) contained approximately 1.5 million cells (12 divisions across gap thickness, 400 at circumferential, 144 in the axial direction, 20x36 in groove cross-sections) with increased mesh resolution near the model walls (see detail view in Fig. 8). The same fluid flow grid was used in all bearing simulations.

3.2.2. Bearing components

In the case of bearing components, the effects of different simplifying model assumptions on the predicted operational bearing properties were investigated using three configurations of FEM grids for bearing components, which differed with shaft and bushing representation. Fig. 9 shows developed models and contains descriptions of applied boundary conditions. To shorten the analysis time, it was assumed that the shaft was non-deformable (it remained cylindrical). This allowed the application of 2D shell-type FEM elements to model the presence

of the shaft in the bearing system (except in the case where heat flow through the shaft was considered). For one configuration ('shell' shaft with the bushing, Fig. 9 b) two different sets of transferred loads at the FSI 2 surface were also realized. This gave four different configurations of the bearing component models, named **Rigid**, **EHD**, **TEHD** and **TEHD full**. The simplest **Rigid** case allowed for investigations of the influence of forced axial flow on thermal phenomena without considering bushing deformations and heat transfer (adiabatic flow). In the **EHD** model, the effect of elastic bushing deformations was also included. The **TEHD** case, in comparison to **EHD**, allowed for heat transfer from the film to the bearing bushing (shaft remained adiabatic). The most advanced ***TEHD full*** model allowed for thermo-elastohydrodynamic analysis of the bearing with consideration of heat transfer from the film through the bushing and shaft. A summary of the model configurations is provided in Table 3. Preliminary calculations proved that heat generation and maximum pressure in the film (maximum deformation of the bushing) appeared at the bottom of the bearing (close to the minimum film thickness). For this reason, the bearing bushing was represented in the model in limited form.

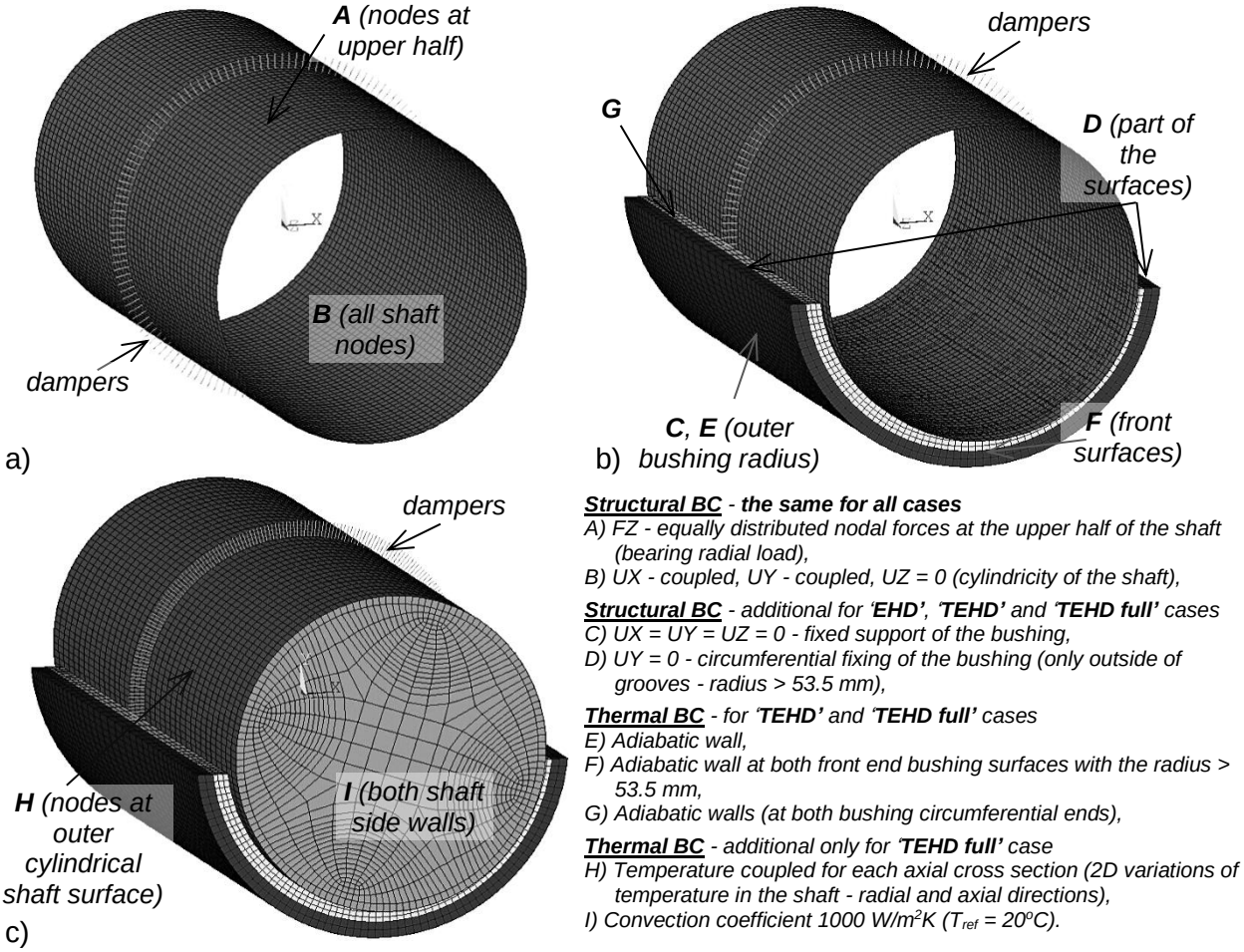

Fig. 9. FEM grids of bearing components in FSI analysis and their boundary conditions (marked schematically); a) Rigid, b) EHD and TEHD, c) TEHD full.

Table 3. Comparison of configurations for bearing components models.

bearing solids model	solids representation		transferred quantities		comment
	shaft	bushing	FSI 1	FSI 2	
Rigid	rigid, shell	-	forces, displacements	-	rigid shaft and bushing, without heat transfer, adiabatic water flow
EHD		lower part, two layers		forces, displacements	rigid shaft, elastic bushing, without heat transfer, adiabatic water flow
TEHD				forces, displacements, temperature, heat flux	rigid shaft, elastic bushing, heat transfer at film/bushing interface
TEHD full	rigid, solid		forces, displacements, temperature, heat flux	forces, displacements, temperature, heat flux	rigid shaft, elastic bushing, heat transfer at film/bushing and film/shaft interfaces

Only the bottom part of the bushing was included (between grooves at angular range 180 and 0°) with only two layers (PTFE and Rubber). The third brass layer was omitted because it has a relatively high value of elastic modulus and thermal conductivity and low thermal expansion comparing to PTFE and Rubber. For this reason, the brass layer has only little effect on thermo-elastic deformations and the temperature field in the bushing. The reference temperature assumed for thermal strain calculations was 20°C. The materials were assumed isotropic and linear-elastic and their parameters used in the analysis are collected in Table 4.

Table 4. Material properties of the bearing components assumed for FSI analysis

parameter		PTFE	Rubber	Steel (shaft)
Young modulus	[MPa]	770	40	2.1×10^5
Poisson number	[-]	0.46	0.497	0.3
thermal expansion	[1/K]	124×10^{-6}	170×10^{-6}	-
density	[kg/m^3]	2100	1200	7810
thermal conductivity	[W/mK]	0.19	0.25	50
specific heat	[J/kg K]	1000	1960	470

To improve the convergence of the FSI solution, it was necessary to slow down movements of the shaft. That was done by using artificial damping introduced to the model with the use of damping elements (evenly distributed around the shaft at mid-length, see Fig. 9). That idea was previously applied with success for analysing hydrodynamic bearings using FSI [29,31]. Those elements were connected to the shaft at one end; the other end was fully constrained. The damping elements did not affect the final results because they did not introduce forces into the system when the equilibrium position was reached. The initial position of the shaft was selected after initial calculations as 20 μm of initial minimum film thickness with attitude angle $\gamma = 35^o$ for the **Rigid** case and 10 μm and $\gamma = 27^o$ for the other cases. The bearing bushing grid contained 14400 3D solid elements (SOLID226) and a shaft of 7200 2D shell elements (SHELL181) or 30528 3D solid elements (SOLID226).

The analyses were performed with the use of high efficient workstation (2 CPU's, 14 cores each, 2 threads/core). Runtime depended on the case and was equal to about a day for the simplest model (Rigid) up to about 6 weeks for the most complex bearing model (TEHD).

4 Results and Discussion

4.1 Results of experimental research

As an example of the experimental results, measurements for one set of bearing operating conditions (n = 3000 rpm and p_m = 0.4 MPa) and different water supply flow rates Q_{in} is shown in Fig. 10 (results for other loads and speeds had similar trends). A case with a typical load level for water lubricated bearings with the highest shaft speed tested (clear thermal effects) was selected for further detailed discussion. All results were summarised, at the end of this section, with the use of proposed diagram of safe bearing operation under limited lubrication.

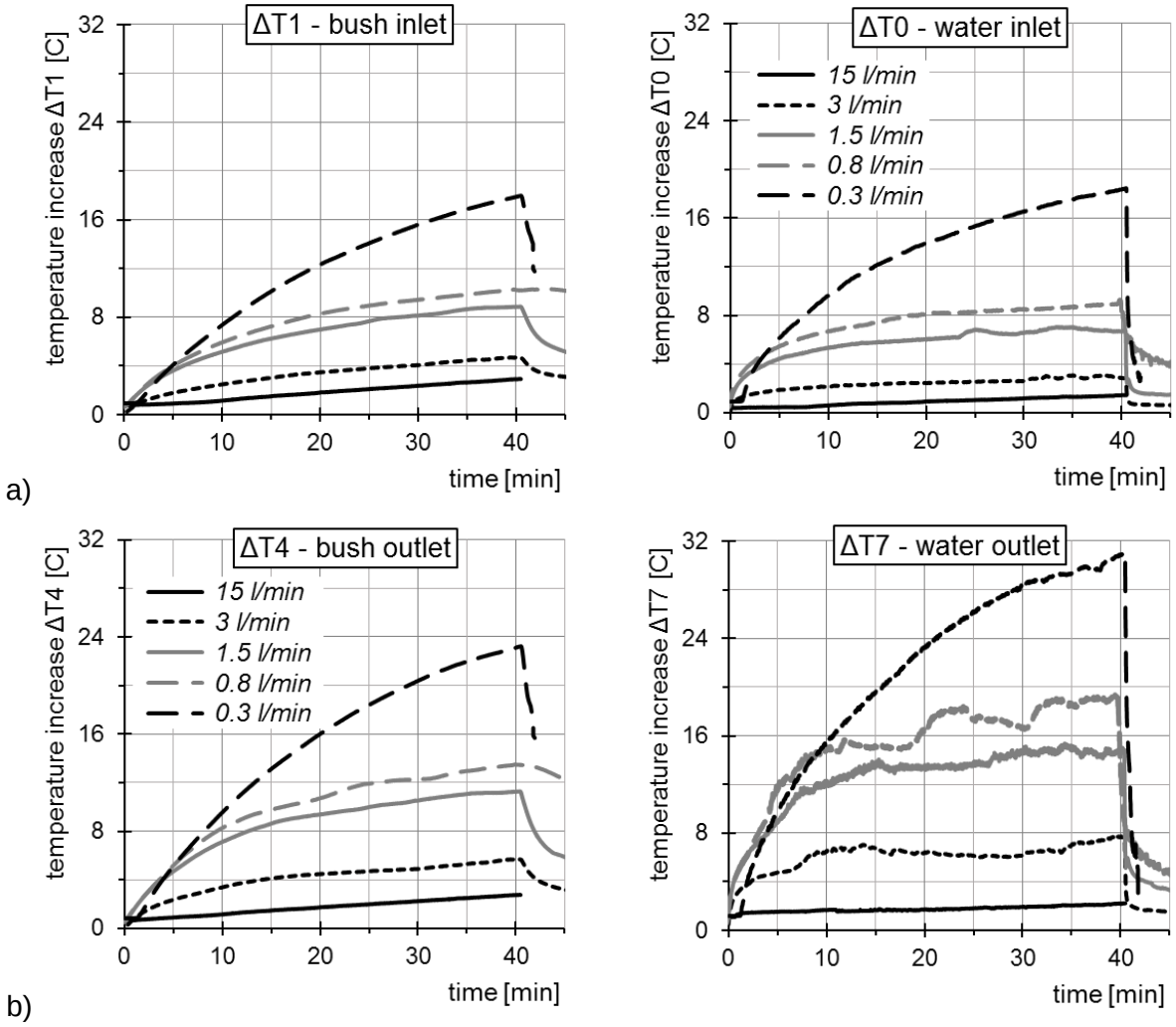

Fig. 10. Temperature increase over T_{in} measured for the bushing (left-hand side) and lubricating water (right-hand side); a) at the inlet, b) at the outlet.

Fig. 10 shows the difference of measured temperature (for bearing bushing and water at inlet and outlet) and water supply temperature. This is helpful to compare the results of measurements in the case when differences in supplying water temperature were recorded (±1°C). Analysis of the collected data revealed that differences between bushing temperatures measured at cross-section B-B (Fig. 3, close to water inlet to the housing: T1, T2 and T3) were not more than 1.5°C. The same was observed for bushing temperatures at cross-section A-A (close to the water outlet from the housing: T4, T5 and T6). Taking this into account, it was reasonable to show only one measured temperature for each of the bushing cross-sections.

Temperatures T1 (B-B - close to the inlet) and T4 (A-A - close to the outlet) measured at the bushing bottom were selected for further analysis.

Collected test results show a significant effect for forced axial water flow on water and bearing bushing temperatures. The lowest temperatures were measured for Q_{in} = 15 l/min. The highest temperatures were noticed for the minimum flow Q_{in} = 0.3 l/min - this case was considered as the last one assuring safe operating conditions of the bearing, according to defined criteria (described with the use of Fig. 5). Reducing axial water flow caused a gradual increase in the measured temperature. The highest temperatures were recorded for the smallest water flow rate (max. bush ΔT4 ~13°C, max. water outlet ΔT7 = ~19°C). Changes in measured temperatures in the bearing bushing were smooth, whereas in lubricating water at the outlet, rapid changes were clearly visible as wavy irregular shapes (for $Q_{in} \leq 3$ l/min, Fig. 10 b). That type of temperature course is characteristic of mixed friction. Moreover, the measured water temperature increase at the inlet to the bearing was noticeably higher than the water supply temperature, especially for lower values of Q_{in} (max. ΔT0 = ~9°C for Q_{in} = 0.8 l/min, Fig. 10 a), which suggests that in the inlet zone, mixing the hot water outflowing from the gap and cold water supplied from the tank could take place as well heat convection from the test stand shaft as a result of its cooling.

Using the temperature measurements presented in Fig. 10, it was also possible to analyse axial temperature increases in the bearing system. The measured axial temperature increase in the bearing bushing (a) and lubricating water (b) are presented in Fig. 11.

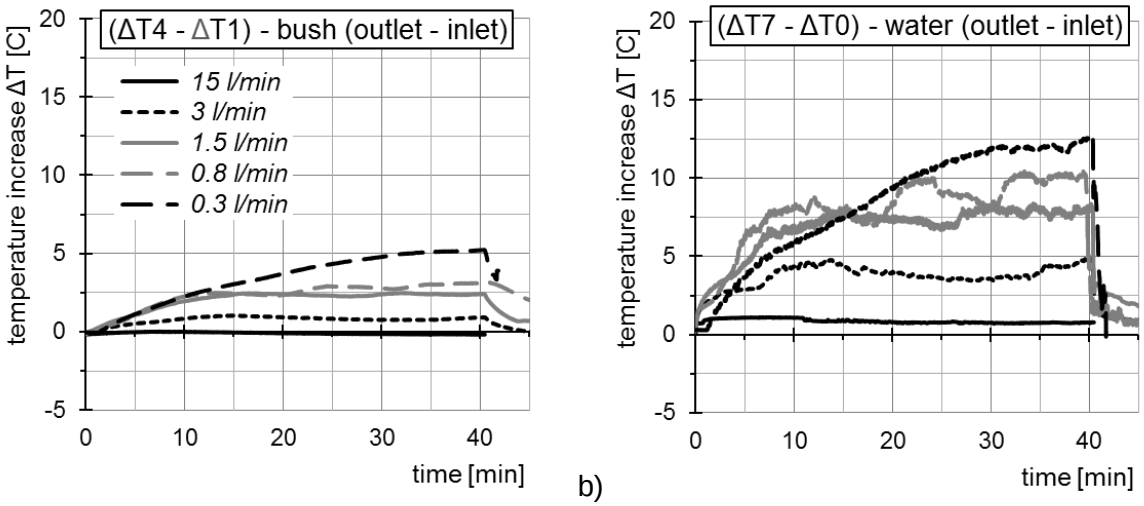

Fig. 11. Measured axial temperature increase; a) in the bearing bushing, b) in the lubricating water.

In the case of the bearing bushing, one can notice that except for Q_{in} = 15 l/min, the bushing was slightly hotter close to the lubricating water outlet compared to its cross-section close to the water inlet. The difference of axial temperatures increased with the decrease of axial water flow rate and was the biggest for the case with the smallest enforced axial water flow. In the case of Q_{in} = 15 l/min, temperatures at both bearing bush cross-sections were comparable - no axial temperature increase was measured. The measured axial lubricating water temperature increase between the outlet and inlet was higher than for the bearing bushing. This is reasonable since water temperature rise can also be a measure of total bearing friction power losses.

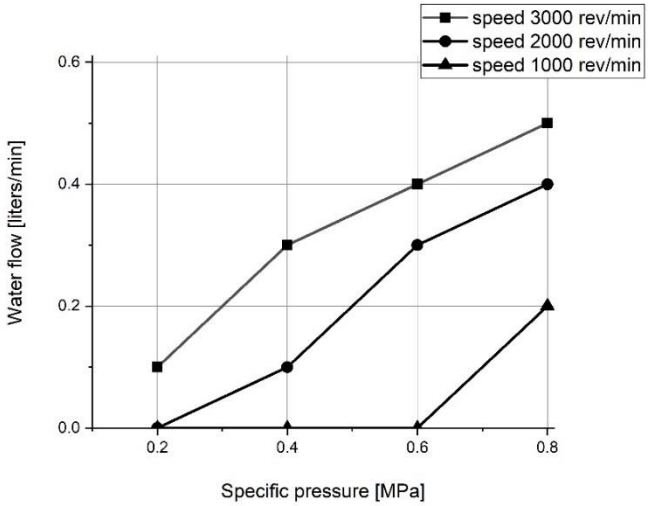

Fig. 12. Diagram of safe operation under limited water axial flow for a 3-layer bearing.

A diagram of safe operation for the tested bearing under limited axial water flow and a wide range of bearing operating conditions is presented in Fig. 12. The results proved that for lowest shaft speed (1000 rpm), a bearing could operate even without axial water flow up to 0.6 MPa load. Increases in the shaft speed caused a decrease in the bearing safe operation area. In conditions of 3000 rpm shaft speed, the bearing did not pass a safety operation test even for the lowest value of bearing load. This revealed that in such cases, forced axial water flow was required to assure safe bearing operation.

4.2 Results of theoretical research

Theoretical analysis was focused on an attempt to explain the course of thermal phenomena, which were observed during experimental tests and also on the research of the most important factors influencing them. Theoretical investigations were divided into two parts. In the first part, thermal effects connected with water flow in the gap and in grooves were analysed. It was carried out using the 'Rigid' model with a simplified representation of the bearing bushing and shaft and adiabatic water flow. The second part contains the results of investigations of the influence of different simplifications implemented for bearing components in the FSI model on the predictions of thermal phenomena accompanying operation of the bearing system.

4.2.1. Effect of the water flow

Investigations of the effect of the water flow in the stern tube bearing on its properties with special attention to thermal effects and the influence of forced axial flow were carried out using the 'Rigid' model. The operational parameters for calculating bearing properties were 3000 rpm rotational speed and 0.4 MPa specific pressure (the same as for the experimental tests results discussed in 4.1).

The main difference in the design of the stern tube bearing in comparison to a classical cylindrical bearing is axial grooves. The aim of the initial calculations was to evaluate the influence of those grooves on the flow phenomena in the gap, including fluid film shearing and the consequential generation of heat. Calculated temperature profiles are shown in Fig. 13 for the case without forced axial water flow through the bearing. It was done assuming the opening

boundary condition (with 20°C opening temperature) on both fluid model sidewalls (Fig. 8). That configuration allowed for a free inflow of the cold water to the bearing from both ends.

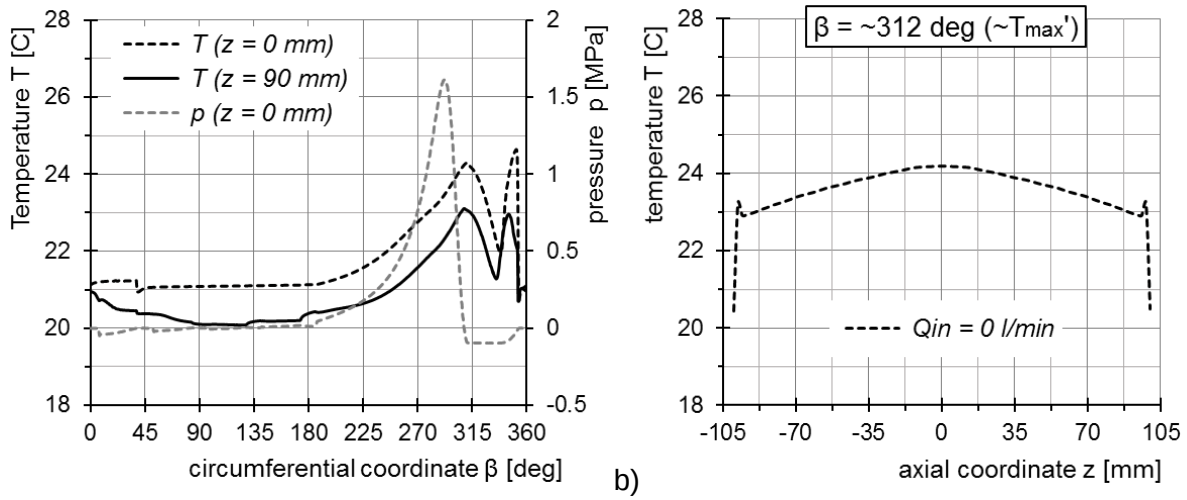

Fig. 13. Calculated temperature and pressure profiles at mid-thickness of the film for the case without forced axial flow; circumferential (a) and axial for Tmax' angular position (b).

The highest temperatures were calculated at the lower half of the bearing bushing (180° < β < 360°, Fig. 13 a). However, the maximum temperature increase over the supply temperature was relatively small (T_{max} = 24.7°C), which is reasonable considering the low water viscosity. Circumferential temperature profiles were influenced by negative film pressure (pressure profile shown in Fig. 13 a). In that zone (308° < β < 360°), flow with cavitation was observed, which caused the local gap temperature drop and, as a consequence, two temperature peaks could be noticed, T' at β = ~314° and T" at β = ~345° (close to the axial lubricating groove). The phenomenon of decreased temperature in the negative pressure zone was also described in other works [24,35]. In the analysed case, it is clearly visible, since the overall temperature rise is relatively low. The radial temperature profile (for T' angular position) showed that the maximum temperature was obtained at the midplane of the bearing.

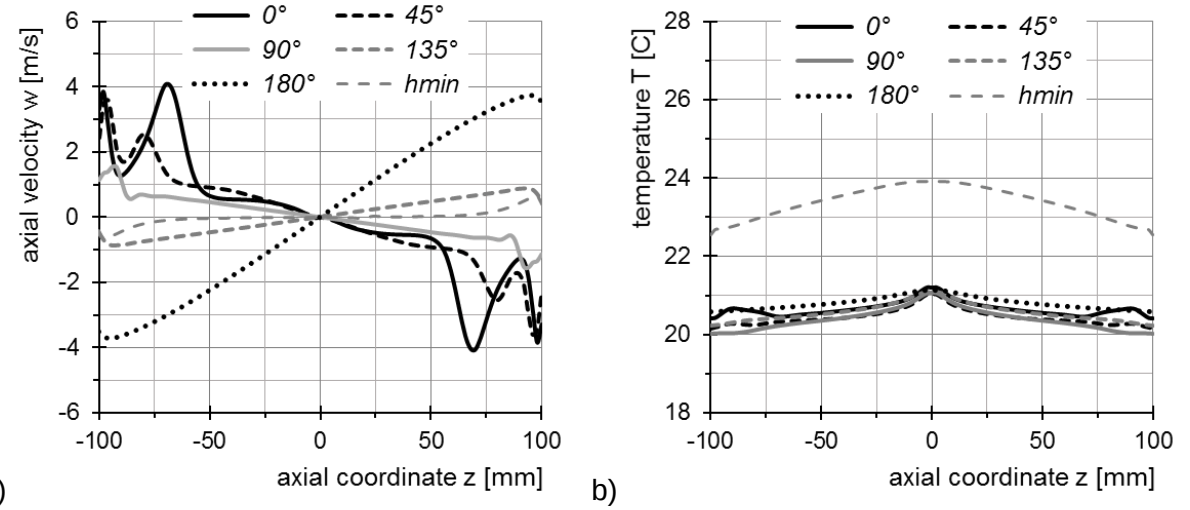

Fig. 14. Calculated flow parameters in the grooves and film for the case without forced axial flow (axial profiles); a) axial flow velocity w [m/s], b) temperature T [°C].

The calculated bearing operational parameters allow one to state that in such conditions, the bearing could work without excessive temperature rise; however, that would only possible due

to the fact that inflow of cold water to the gap was possible. In Fig. 14 a), axial velocity profiles in grooves (for the central point of their cross-section) and for minimum film thickness position ($\gamma = 32^o$, film mid thickness, $h_{min} = 9.6$ μm) are shown. In Fig. 14 b), the calculated water temperatures at those locations were presented.

The obtained profiles are symmetrical with the symmetry axis on the middle of the bearing length (z=0 mm). There is no axial flow through the whole bearing length (from one end to the other). The axial velocity of the water in the grooves is several times bigger than in the gap. There is also a kind of axial circulation of the water. The inflow took place by grooves 0°, 45° and 90° (those grooves are in the divergent part of the gap), while outflow took place by grooves 135° and 180° (those grooves are in the convergent part of the gap). It is clearly visible, that significant flow was calculated through the grooves since they have small resistance to flow compared to the gap. The temperature in grooves is low due to the suction of cold water at the side ends of the bushing. That bearing configuration is only a theoretical example; however, it was very useful to explain and demonstrate the phenomena accompanying stern tub bearing operation.

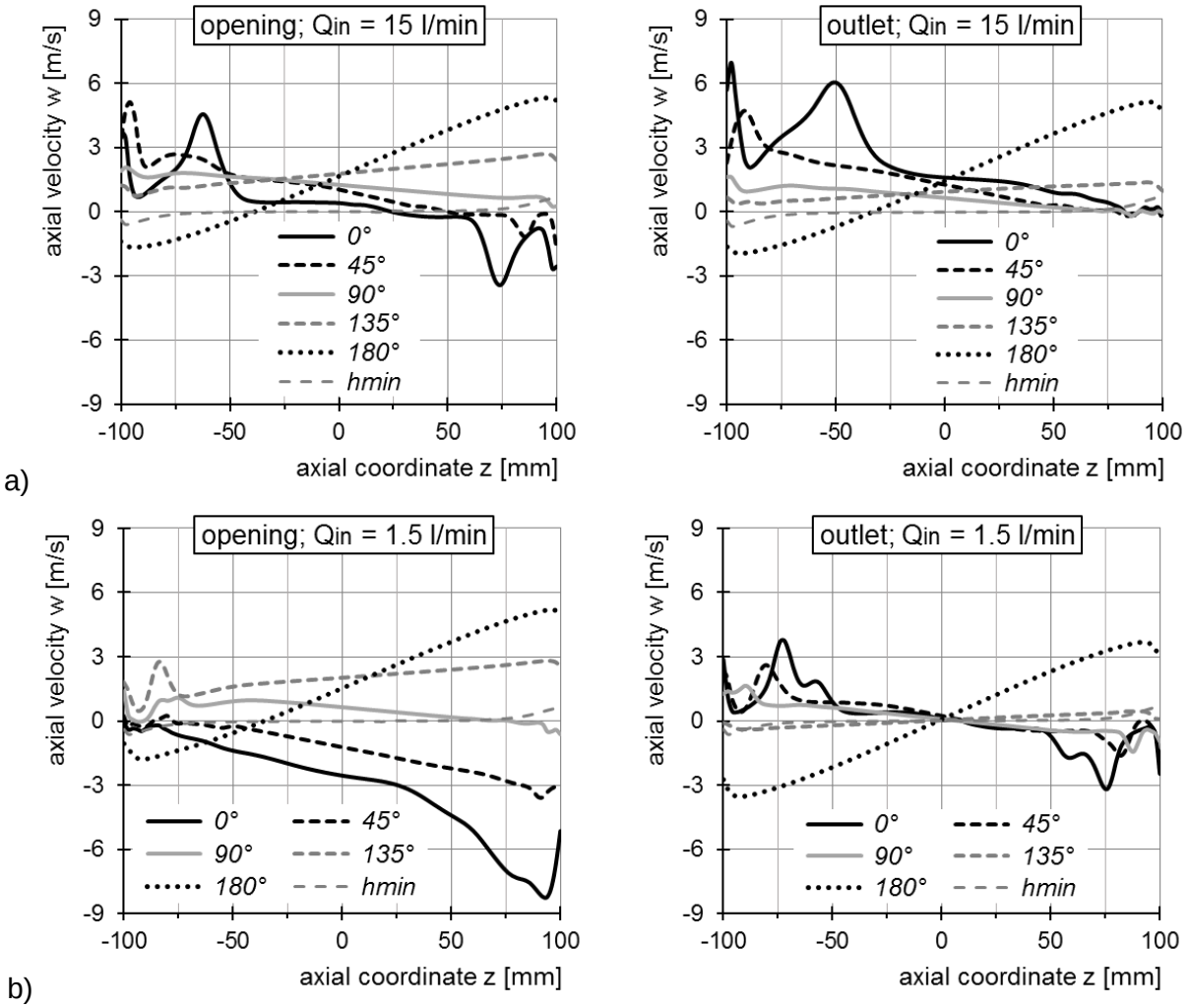

Fig. 15. Axial flow velocity w [m/s] profiles in the grooves and at the minimum thickness of the film for different boundary conditions at the outlet; a) Q_{in} =15 l/min, b) Q_{in} = 1.5 l/min.

Flow conditions at the inlet and outlet zones of the bushing could have a strong impact on bearing properties. In the tested bearing, at the inlet zone, enforced water flow Q_{in} was imposed. An investigation of the effect of boundary condition at the outlet zone on phenomena accompanying bearing operation was carried out using theoretical calculations. Two types of outlet conditions were studied: opening with a 20ºC opening temperature and outlet. The opening boundary condition allowed for the inflow of the water at 20°C to the fluid domain, whereas using the outlet condition, only outflow from the domain was possible. Calculations were done for two values of the enforced water flow Q_{in}, differing by an order of magnitude, to highlight differences in the flow phenomena, 15 l/min nominal and 1.5 l/min reduced. In Fig. 15 and Fig. 16, the results of calculated axial velocities of the water in grooves and along the film (at h_{min}) are compared. In Fig. 17, temperature profiles of the fluid are also shown (circumferential and axial).Calculated axial flow velocity profiles in the grooves for nominal flow Q_{in} = 15 l/min were similar for both types of boundary conditions at the outlet (Fig. 15 a). However, there were small differences, such as, for example, in the 'opening' case. There was backflow calculated to the grooves at 0° - 45° angular position, while in the 'outlet' case of it was not visible and water flow had one direction (from inlet to outlet - except the axial range -100 mm < z < -30 mm for groove 180°). As opposed to the nominal flow case, a comparison of the axial velocities for reduced enforced water flow Q_{in} = 1.5 l/min showed significant differences (Fig. 15 b). For the 'opening' boundary condition, backflow with high values of axial velocity was calculated in grooves 0° and 45° (up to ~ -9 m/s, z=100 mm), while in the case of 'outlet', axial velocity profiles were very similar in shape to profiles calculated for a bearing without enforced axial flow (see Fig. 14 a). They were almost symmetric, with the symmetry axis in the mid bearing length, and with visible backflows (grooves 0–90°, z > 0 mm).

Backflow phenomenon was also show in Fig. 16, which compares calculated axial velocity fields for groove 0º and two water flow intensities. It is clearly visible, that in case of Q_{in}= 1.5 l/min, flow in the groove close to outlet zone runs in the opposite direction to the enforced direction (along Z axis).

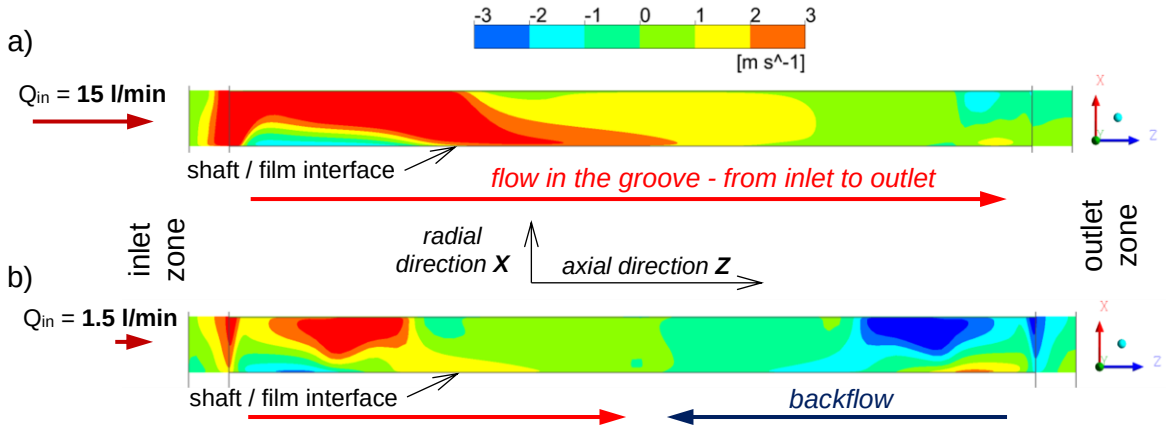

Fig. 16. Comparison of axial velocity field w [m/s] for groove 0º (horizontal cross section, top view) obtained with the 'outlet' boundary condition (length of the groove reduced 4 times to enhance readability); a) Q_{in} =15 l/min (top profile), b) Q_{in} = 1.5 l/min (bottom profile).

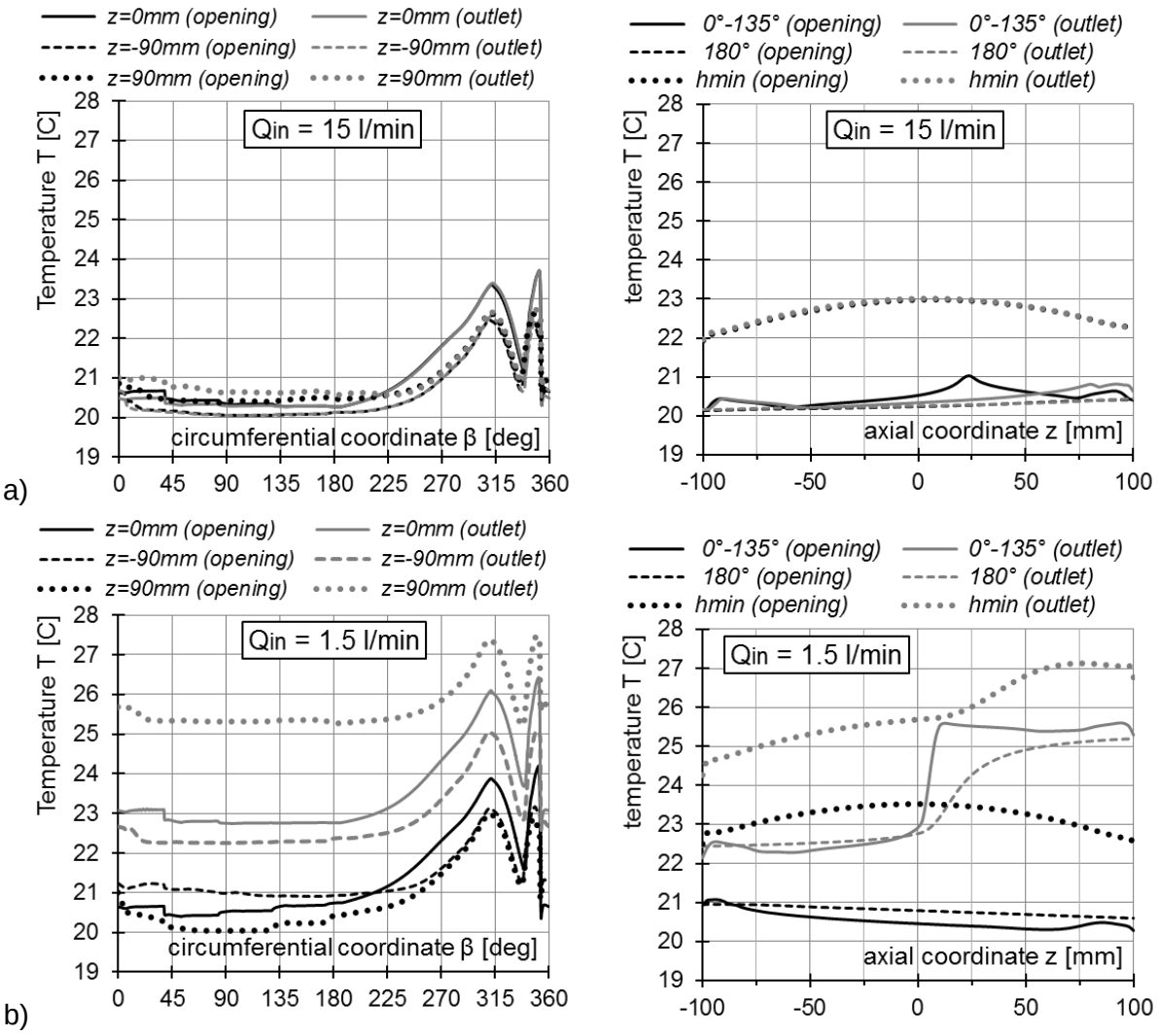

Fig. 17. Temperature profiles [C] (circumferential – left-hand side, axial – right-hand side) of the water in the grooves and film for different boundary conditions at the outlet; a) Q_{in} =15 l/min, b) Q_{in} = 1.5 l/min (calculated temperatures in the grooves 0°-135° were very similar irrespective of its angular position, so they were shown with only one line).

The calculated flow structure was reflected in the results of water temperatures in the grooves and film. For a nominal enforced axial flow of 15 l/min, temperature profiles obtained using both types of boundary conditions at the outlet were very similar (Fig. 17 a) because, in both cases, flow similarity took place (Fig. 15 a). The highest temperature was calculated in the midplane of the bearing, the temperature in the grooves was low and increased slightly starting from 20°C at the bushing border close to the inlet (z=-100mm) to ~20.5°C at the bushing outlet. That is in good agreement with measurement results.

A significant difference in the flow structure for a reduced axial flow of 1.5 l/min was obtained for both types of boundary conditions at the outlet, resulting in differences in calculated temperature field in the gap. In the case of 'opening' boundary conditions, slightly lower temperatures were calculated close to the outlet zone from the bushing due to the effect of cold-water suction through grooves to the gap. The maximum temperature was obtained close to the bearing midplane (T_{max} = 24.2°C). The temperature field calculated using the 'outlet' boundary condition differs significantly. The lowest temperatures were calculated at the bushing end close to the water inlet zone. It is worth noting that the water temperature at the

inlet to the grooves was higher than the supply water temperature (~22°C), the same as was observed in the experiment results. A step change of the water temperature in the grooves could be observed in the mid-length of the bearing. The highest temperatures were calculated in the film close to the bushing outlet zone. Similar bushing temperature axial profiles (lowest temperature close to the inlet, highest close to outlet) were recorded during experimental tests. That is evidence, that the 'outlet' boundary condition implemented in fluid model better describes conditions in the outlet zone, which took place during bearing experiments.

A summary of calculated bearing parameters as a function of axial water flow and imposed boundary condition in the outlet zone is provided in Table 5. For all analysed cases, the obtained minimum film thickness was not more than 10 μm, which does not guarantee fluid film friction for real water-lubricated bearing operation. Only small differences between analysed cases were observed in the calculated value of attitude angle and maximum pressure value, except the case of 1.5 l/min reduced flow and 'outlet' boundary condition, for which the maximum pressure was higher. This is probably due to the higher film temperature and consequently lower minimum film thickness.

Table 5. Calculated properties of the bearing for different Q_{in} flows for both types of imposed boundary conditions in the outlet zone.

parameter			opening BC		outlet BC	
			15 l/min	1.5 l/min	15 l/min	1.5 l/min
minimum film thickness	[μm]	h_{min}	9.9	9.7	9.7	8.9
attitude angle	[deg]	γ	33.2	33.5	34.1	33.5
maximum film temperature	[°C]	T_{max}	23.7	24.2	23.7	27.8
maximum film pressure	[MPa]	p_{max}	1.61	1.62	1.64	1.75

4.2.2. Effect of bearing components

Investigations of the effect of bush and shaft modelling on water-lubricated stern tube bearing properties were carried out for the case of 3000 rpm and 0.4 MPa operating conditions with Q_{in} = 1.5 l/min forced axial flow and assuming the 'opening' type boundary condition at the outlet zone of the fluid model. The applied models allowed to investigate the effects of bushing elasticity (EHD model), combined bushing elasticity with heat transfer through it (TEHD model) and combined bushing elasticity and heat transfer through the bushing and shaft on thermal phenomena during bearing operation ('TEHD full' model).

In Fig. 18, sliding surface radial bushing deformation (a), temperature (b) and pressure (c) profiles calculated using different models were compared at the midplane of the bearing and at selected axial cross-sections.

The calculated profiles of bushing radial deformations were similar in shape for all models that considered its elasticity. The bushing is compressed due to the high pressure in the film; as a result, a concave sliding surface shape was obtained (positive value of ΔR parameter, see the coordinate system in Fig. 1). However, for TEHD, model thickening of the bush wall could be observed (a negative value of radial deformation ΔR means increased thickness). This is caused by heat transfer through the bushing in the TEHD model, which resulted in thermal gradients across the bushing wall thickness. A relatively small temperature difference across the bushing thickness, due to thermal expansion (with a high value of expansion coefficients), thickened it about 10 μm compared to EHD and 'TEHD full' model results.

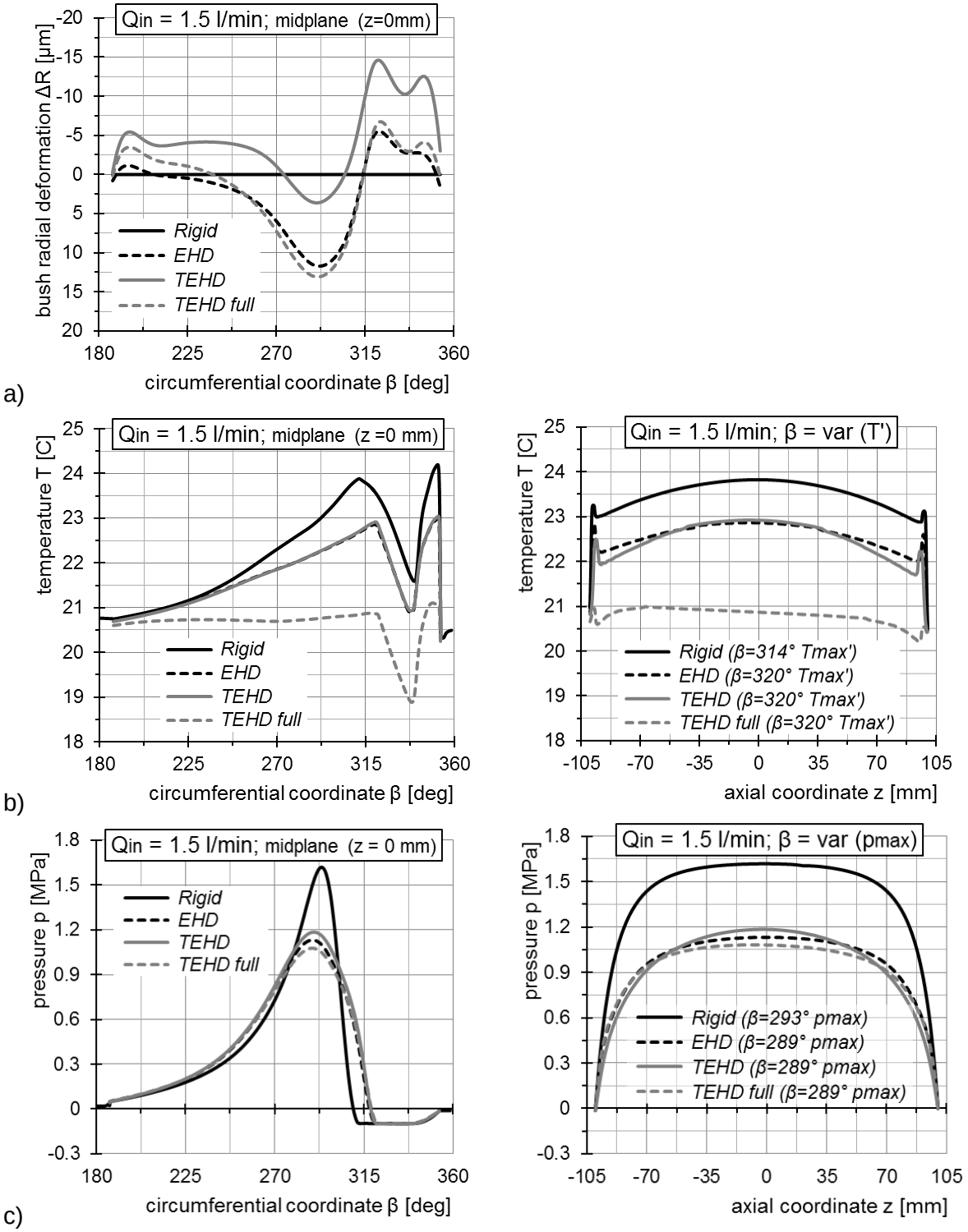

Fig. 18. Calculated profiles: circumferential (left-hand side) and axial (right-hand side) of the bushing sliding surface: radial deformation (a), temperature (b) and film pressure (c).

Heat transfer through the bushing was also included in the 'TEHD full' model, but in this case, most of the heat was removed from the friction zone by convection in the shaft, which results in the lowest calculated temperatures using that model, and in consequence, the maximum temperature was only slightly higher than the water supply temperature (Fig. 18 b). The highest temperature was calculated using the Rigid model, whereas the bushing elasticity and heat transfer from the gap (mainly by the shaft) reduce it. Bushing deformations also influenced film

pressure profiles; the maximum pressure for those cases was significantly lower in comparison to the Rigid case results. Calculated pressure profiles using EHD, TEHD and 'TEHD full' differed only slightly.

Bearing bushing deformations also changed gap geometry significantly. Calculated film thickness profiles are compared in Fig. 19. The minimum gap thickness from all investigated cases was calculated using the Rigid model. When bushing deformation was included, the minimum gap thickness was slightly thicker and was obtained close to the bushing edge.

The calculated parameters of the bearing operation using bearing models differing by assumptions for bushing and shaft are presented in Table 6. Bearing bushing mechanical deformations significantly influenced the shaft position (attitude angle γ), maximum film pressure and calculated bearing friction torque. When heat transfer was considered through the bushing (TEHD model) thermo-mechanical deformations were advantageous for minimum film thickness, which was calculated as 13.4 μm (the biggest from all analysed cases).

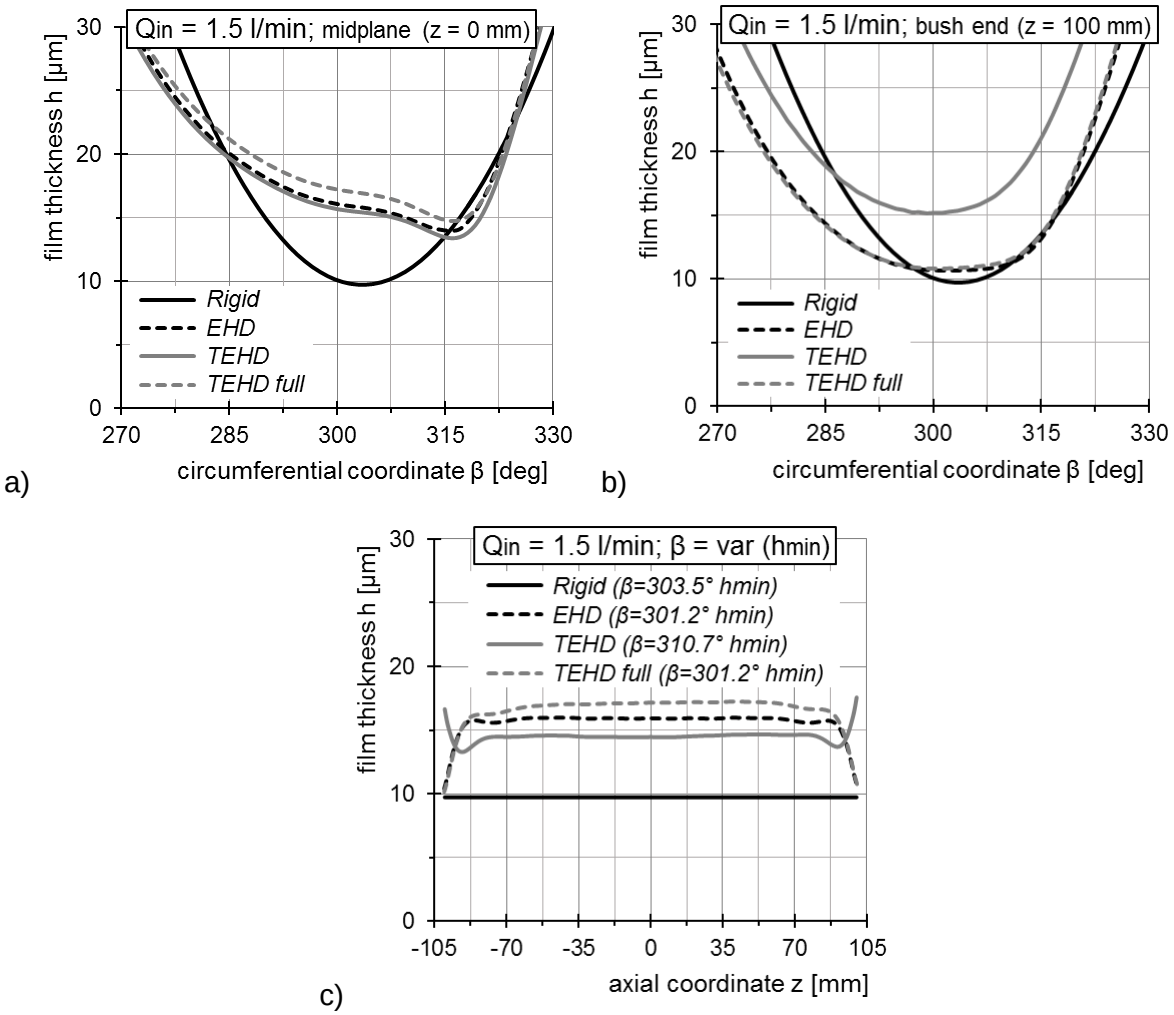

Fig. 19. Calculated gap thickness profiles; circumferential at the midplane (a) and at the bush end (b) and radial (c) obtained using different assumptions for the bearing bushing.

Table 6. Calculated properties of the bearing using different models (Q_{in} = 1.5 l/min)

parameter			Rigid	EHD	TEHD	TEHD full
minimum film thickness	[μm]	h_{min}	9.7	10.4	13.4	10.2
attitude angle	[deg]	γ	33.5	26.5	26.0	25.9
maximum film temperature	[C]	T_{max}	24.2	23.0	22.9	21.4
maximum film pressure	[MPa]	p_{max}	1.62	1.13	1.18	1.08
friction torque	[Nm]	M_f	1.78	1.68	1.68	1.69

4.2.3. Discussion of the Results

Experimental studies showed that axial water flow has a significant impact on recorded bearing temperature. Under nominal water axial flow, measured temperatures were only slightly higher than the water supply temperature. Reducing the axial flow resulted in an increase of bushing and water temperature at the inlet and outlet zones. The temperature of the bearing bushing closer to the water inlet to the bearing were lower than those closer to the outlet. Additionally, for reduced axial water flow, the measured inlet water temperature was higher than the water supply temperature. As a result of a comprehensive experimental measurement program, a bearing safe operation diagram was defined. This diagram indicates operating conditions that are acceptable for a temperature increase of the bearing in limited water axial flow operation. According to the experimental results, a three-layers stern bearing was able to operate even without forced axial flow for low speed and low load conditions.

Theoretical studies showed a close relationship between the structure and direction of water flow in the grooves and the course of thermal phenomena accompanying its operation. Under nominal lubricating water flow, the inlet water supply to the bearing flowed through the entire bearing (mainly in the grooves) in one direction (from inlet to outlet). There was no suction of water from the outlet zone back into the bearing gap through the grooves (no backflow). This resulted in low bearing operational temperature because the heat generated due to shearing the film was removed from the gap by water flowing in the axial direction.

However, as the theoretical analysis results showed, under the conditions of operation with reduced forced axial water flow through the bearing, there is a phenomenon of water backflow. It relies on water suction from the outlet space and inlet space through the grooves back into the lubrication gap. The back-flowing water had a temperature higher than the supply temperature as a result of mixing the hot water flowing out of the gap into the outlet space and inlet space and re-entering into the bearing. This results in an increase of the bearing bushing temperature at the inlet and outlet; however, the highest temperatures were calculated close to the bearing outlet zone. The obtained results of theoretical investigations using suitable boundary conditions in the outlet zone, which allowed for considerations of the water backflow phenomenon (flow model with 'outlet' boundary condition), are in good agreement with the trends observed in experimental studies.

In theoretical tests of bearings with axial grooves and in conditions of limited axial water flow, special attention should be paid to considering the inlet and outlet areas. The imposed boundary conditions should reflect conditions from the real bearing operation and allow for mixing the water outflowing from the gap and for its backflow into grooves. This is of high importance since the boundary condition at the outlet zone has a strong influence on the

calculation results for stern bearings with axial grooves, especially for the case when reduced forced axial flow is considered.

According to the theoretical results, the bushing elasticity and heat flow through the bushing do not significantly change the course of thermal phenomena in the bearing. It is different when the heat flow through the bearing shaft is considered since taking this phenomenon into account significantly affects the calculated bearing system temperature. This is due to the very high thermal conductivity of the shaft and large thermal capacity (steel) compared to the bushing materials (PTFE and Rubber). It should be mentioned, however, that further analysis should be carried out on the impact of the arbitrarily adopted convection boundary condition at the shaft ends (the 'TEHD full' model) on the obtained calculation results.

A comparison of the calculated temperature values and those measured for the condition of limited water flow through the bearing indicates that the measured values are higher than the calculated values. As an example, for a reduced axial flow of 1.5 l/min, the bearing temperature increase was a maximum of about 8°C at the inlet (ΔT1) and 11°C at the outlet (ΔT4; Fig. 10), while the calculated temperature increases were only around 2.5°C (inlet) and 5.5°C at the outlet (Fig. 17 b).

The probable reason for the disagreement between theoretical and experimental results is that the tested bearing could work in a mixed lubrication regime. This was reasonable considering the calculated minimum film thickness (~10 μm). Further evidence of that mode of friction is found in the wavy irregular shapes of the measured water temperature at the outlet. Mixed friction is characterized by a much more intense heat generation and temperature increase compared to hydrodynamic friction, which was assumed in the theoretical research. That could explain the differences between calculated and measured bearing temperatures. The occurrence of mixed friction in the bearing can be caused by bushing hole shape errors (cylindricity errors) or misalignment of the bushing and shaft axes.

5 Conclusions

The paper contains the results of experimental and theoretical studies of thermal effects accompanying the operation of a water-lubricated stern bearing, including the effect of reduced forced axial flow. The main findings of the research can be summarised as follows:

- temperature of water-lubricated bearing with axial grooves depends significantly on intensity of enforced axial flow,
- according to proposed bearing safe operation diagram, the tested bearing was able to operate even without enforced axial water flow (in conditions of low speed and load),
- as results of theoretical investigations show, proper modelling of water flow conditions at the bearing sides is of great importance,
- nominal axial flow assures water flow in grooves in one direction, from the inlet to the outlet zone,
- restricted axial flow promotes a water backflow phenomenon (from bearing side zones to the grooves) with temperature higher than the supply one, which plays a decisive role in the bearing's temperature increase,
- theoretical results reveal, that bushing's elasticity and heat flow through the bushing do not significantly alter thermal effects in the lubricating film, whereas the heat transferred through the shaft strongly affects the temperature of the whole system.

6 Acknowledgements

This work was a part of research grant no. 2016/23/B/ST8/03104 entitled “Research on water-lubricated sliding couples in unfavourable operating conditions” financed by the Polish National Science Centre.

7 References

[1] Thordon Engineering Manual Version E2006.1. Thordon Bearings Inc.; 2006.

[2] Yamajo S, Kikkawa F. Development and application of PTFE compound bearings. Dyn. Position. Conf., Houston, USA: 2004, p. 1–18.

[3] Lee J. Application of strain gauge method for investigating influence of ship shaft movement by hydrodynamic propeller forces on shaft alignment. Meas J Int Meas Confed 2018. doi:10.1016/j.measurement.2018.02.067.

[4] Hirani H, Verma M. Tribological study of elastomeric bearings for marine propeller shaft system. Tribol Int 2009. doi:10.1016/j.triboint.2008.07.014.

[5] Litwin W, Olszewski A, Wodtke M. Influence of shaft misalignment on water lubricated turbine sliding bearings with various bush modules of elasticity. Key Eng Mater 2011;490:128–34. doi:10.4028/www.scientific.net/KEM.490.128.

[6] Litwin W. Properties comparison of rubber and three layer PTFE-NBR-bronze water lubricated bearings with lubricating grooves along entire bush circumference based on experimental tests. Tribol Int 2015. doi:10.1016/j.triboint.2015.03.039.

[7] Litwin W. Water lubricated marine stern tube bearings - Attempt at estimating hydrodynamic capacity. Proc. ASME/STLE Int. Jt. Tribol. Conf. 2009, IJTC2009, 2010. doi:10.1115/IJTC2009-15068.

[8] Dong C, Shi L, Li L, Bai X, Yuan C, Tian Y. Stick-slip behaviours of water lubrication polymer materials under low speed conditions. Tribol Int 2017. doi:10.1016/j.triboint.2016.10.027.

[9] Litwin W, Olszewski A. Assessment of possible application of waterlubricated sintered brass slide bearing for marine propeller shaft. Polish Marit Res 2012. doi:10.2478/v10012-012-0040-4.

[10] Yuan C, Guo Z, Tao W, Dong C, Bai X. Effects of different grain sized sands on wear behaviours of NBR/casting copper alloys. Wear 2017. doi:10.1016/j.wear.2017.02.019.

[11] Dong CL, Yuan CQ, Bai XQ, Yang Y, Yan XP. Study on wear behaviours for NBR/stainless steel under sand water-lubricated conditions. Wear 2015. doi:10.1016/j.wear.2015.01.009.

[12] Wood RJK. Marine wear and tribocorrosion. Wear 2017. doi:10.1016/j.wear.2017.01.076.

[13] Litwin W, Dymarski C. Experimental research on water-lubricated marine stern tube bearings in conditions of improper lubrication and cooling causing rapid bush wear. Tribol Int 2016. doi:10.1016/j.triboint.2015.12.005.

[14] Zhang X, Yin Z, Jiang D, Gao G, Wang Y, Wang X. Load carrying capacity of misaligned hydrodynamic water-lubricated plain journal bearings with rigid bush materials. Tribol Int 2016. doi:10.1016/j.triboint.2016.02.038.

[15] Armentrout RW, He M, Haykin T, Reed AE. Analysis of Turbulence and Convective Inertia in a Water-Lubricated Tilting-Pad Journal Bearing Using Conventional and CFD Approaches. Tribol Trans 2017. doi:10.1080/10402004.2016.1251668.

[16] Gao G, Yin Z, Jiang D, Zhang X. Numerical analysis of plain journal bearing under hydrodynamic lubrication by water. Tribol Int 2014. doi:10.1016/j.triboint.2014.03.009.

[17] Mallya R, Shenoy SB, Pai R. Static characteristics of misaligned multiple axial groove water-lubricated bearing in the turbulent regime. Proc Inst Mech Eng Part J J Eng Tribol

2017. doi:10.1177/1350650116657757.

[18] Gao G, Yin Z, Jiang D, Zhang X, Wang Y. Analysis on design parameters of water-lubricated journal bearings under hydrodynamic lubrication. Proc Inst Mech Eng Part J J Eng Tribol 2016. doi:10.1177/1350650115623201.

[19] Zhang X, Gao G, Yin Z, Wang Y, Gao C. Numerical analysis and experimental research on load carrying capacity of water-lubricated tilting-pad thrust bearings. Mech Ind 2018. doi:10.1051/meca/2018005.

[20] Song Z, Guo F, Liu Y, Liu X, Wang Y. Inertia Effect on the Load Capacity of Large Water-Lubricated Thrust Bearing. Tribol Trans 2018. doi:10.1080/10402004.2016.1275904.

[21] Pai R, Hargreaves DJ. Water Lubricated Bearings. Green Energy Technol 2012. doi:10.1007/978-3-642-23681-5_13.

[22] De C, Zhen-Qiang Y, Ya-Bo X. Study on the water lubricated large-scale tilting pad thrust bearing by finite element method. Lect. Notes Eng. Comput. Sci., 2015.

[23] Liang X, Yan X, Ouyang W, Wood RJK, Liu Z. Thermo-Elasto-Hydrodynamic analysis and optimization of rubber-supported water-lubricated thrust bearings with polymer coated pads. Tribol Int 2019. doi:10.1016/j.triboint.2019.06.012.

[24] Lin X, Jiang S, Zhang C, Liu X. Thermohydrodynamic analysis of high speed water-lubricated spiral groove thrust bearing considering effects of cavitation, inertia and turbulence. Tribol Int 2018. doi:10.1016/j.triboint.2017.11.037.

[25] Li, Hulin, Wang, Yanzhen, Zhong, Ning, Chen, Yonghong, Yin, Zhongwei. Study on the performance of journal bearings in different lubricants by CFD and FSI method with thermal effect and cavitation. MATEC Web Conf 2018;249:3006. doi:10.1051/matecconf/201824903006.

[26] Feng H, Jiang S, Ji A. Investigations of the static and dynamic characteristics of water-lubricated hydrodynamic journal bearing considering turbulent, thermohydrodynamic and misaligned effects. Tribol Int 2019. doi:10.1016/j.triboint.2018.09.007.

[27] Olszewski A, Wodtke M, Hryniewicz P. Experimental investigation of prototype water-lubricated compliant foil bearings. Key Eng Mater 2011;490:97–105. doi:10.4028/www.scientific.net/KEM.490.97.

[28] ANSYS 18.2 Documentation. Swanson Analysis Inc. 2017.

[29] Pajączkowski P. Transient states simulations of large hydrodynamic thrust bearings. PhD thesis. Gdansk University of Technology, 2010.

[30] Laukiavich CA, Braun MJ, Chandy AJ. An Investigation into the Thermal Effects on a Hydrodynamic Bearing's Clearance. Tribol Trans 2015. doi:10.1080/10402004.2015.1023408.

[31] Wodtke M, Olszewski A, Wasilczuk M. Application of the fluid-structure interaction technique for the analysis of hydrodynamic lubrication problems. Proc Inst Mech Eng Part J J Eng Tribol 2013;227. doi:10.1177/1350650113481147.

[32] Lin Q, Bao Q, Li K, Khonsari MM, Zhao H. An investigation into the transient behavior of journal bearing with surface texture based on fluid-structure interaction approach. Tribol Int 2018. doi:10.1016/j.triboint.2017.09.026.

[33] Zhai L, Luo Y, Liu X, Chen F, Xiao Y, Wang Z. Numerical simulations for the fluid-thermal-structural interaction lubrication in a tilting pad thrust bearing. Eng Comput (Swansea, Wales) 2017. doi:10.1108/EC-08-2015-0209.

[34] Liang X, Yan X, Liu Z, Ouyang W. Effect of perturbation amplitudes on water film stiffness coefficients of water-lubricated plain journal bearings based on CFD–FSI methods. Proc Inst Mech Eng Part J J Eng Tribol 2019. doi:10.1177/1350650118818027.

[35] Fundamentals of Cavitation. 2005. doi:10.1007/1-4020-2233-6.